ACETONE DROPLET BEHAVIOR IN REACTING AND NON REACTING TURBULENT FLOW

M. Chrigui[*], J. Gounder[**], A. Sadiki[*], J. Janicka[*], and A.R. Masri[***]
mchrigui@ekt.tu-darmstadt.de
* Institute for Energy and Power plant Technology, TU Darmstadt, Petersenstr, Germany
** Deutsches Zentrum für Luft- und Raumfahrt, Pfaffenwaldring 38, 70569 Stuttgart, Germany
*** School of Aerospace, Mechanical and Mechatronic Eng., University of Sydney, NSW 2006 Australia

Abstract

Acetone droplet characteristics in reacting and non-reacting turbulent flow are predicted and compared to experimental data. The investigation studies effects of surrounding environment properties on the velocities, dispersion, and evaporation of a relatively volatile spray fuel that featured a wide range of Stokes numbers. The spray environment is altered from cold to hot two phase flow by considering combustion. Droplets are generated using an ultrasonic atomizer. It produces a relatively uniform velocity distribution with a moderate carrier to fuel velocities ratio. The simulations are performed in the framework of Reynolds Averaging Navier Stokes equations along with the Eulerian-Lagrangian approach in which 12 different classes of the dispersed phase are tracked. Droplets differed in diameter, mean and rms velocities, and numbers density. The transport equations of the carrier phase are formulated in an Eulerian reference frame that included terms which account for the exchange of mass, momentum, energy and turbulence quantities with the spray, i.e. fully two way coupling. The phase transition was modeled by the Langmuir-Knudsen law that account for non equilibrium effects based on a consistent determination of the molar mass fraction on the droplet surfaces. For the droplet diffusion, the Markov sequence model was improved by adding a correction drift term to the fluid fluctuation velocity at the parcel position along the droplet trajectory. This correction term aimed at accounting for the non-homogeneity effects in the turbulent flow. The combustion is captured using the Bray-Moss-Libby model that is adjusted to account for the partially premixed spray combustion. The chemistry is described with the flamelet model using a recent detailed reaction mechanism that involves 84 species and 409 reactions for which the Lewis number is not set to the unity.

Introduction

Spray characteristics are sensitive to time and space uniformity of the carrier phase variation. These time and space changing fuel properties (in the gas and in liquid phase) affect substantially the vaporization and kinetics-related processes, like ignition, flame propagation/stability and pollutant levels. Crucial issues when designing a gas turbine combustor or IC-engine for liquid fuels are the understanding of flow-liquid interaction and the prediction of the spray distribution. Accurate modeling of these phenomena requires taking into account turbulence, heat transfer and fuel spray evaporation. Considerable outstanding work investigated two phase flow and predicted spray properties [1-9]. This work highlights the differences of dispersed phase characteristics in cold environment and within a partially premixed reacting turbulent two phase flow.

Modeling approaches

Carrier phase modeling

The turbulent fluid phase is described following RANS- modeling approach. For this purpose, the transport equations are solved for mass conservation, momentum, concentration and temperature, i.e. eq. (1)-(4).

$$\frac{\partial \overline{\rho}}{\partial t}+\frac{\partial\left(\overline{\rho u_i}\right)}{\partial x_i}=\overline{S}_{1,p,v}, \tag{1}$$

$$\frac{\partial\left(\overline{\rho u_i}\right)}{\partial t}+\frac{\partial\left(\overline{\rho u_j u_i}\right)}{\partial x_j}=\overline{\rho} g_i-\frac{\partial \overline{p}}{\partial x_i}+\frac{\partial}{\partial x_j}\left(\mu\frac{\partial \overline{u_i}}{\partial x_j}-\overline{\rho u_i' u_j'}\right)+\overline{S}_{u_i,p,s}+\overline{S}_{u_i,p,v}, \tag{2}$$

$$\frac{\partial\left(\overline{\rho y}\right)}{\partial t}+\frac{\partial\left(\overline{\rho u_j y}\right)}{\partial x_j}=\frac{\partial}{\partial x_j}\left(\overline{\rho}\Gamma\frac{\partial \overline{y}}{\partial x_j}-\overline{\rho u_j' y'}\right)+\overline{S}_{y,p,s}+\overline{S}_{y,p,v}, \tag{3}$$

$$\frac{\partial\left(\overline{\rho T}\right)}{\partial t}+\frac{\partial\left(\overline{\rho u_j T}\right)}{\partial x_j}=\frac{\partial}{\partial x_j}\left(\overline{\rho}\Gamma\frac{\partial \overline{T}}{\partial x_j}-\overline{\rho u_j' T'}\right)+\overline{S}_{T,p,s}+\overline{S}_{T,p,v}, \tag{4}$$

For the turbulence description, the *RNG* model which was adjusted for two-phase flows has been considered, i.e. eq. (5) and (6).

$$\frac{\partial k}{\partial t}+\frac{\partial}{\partial x_i}\left(\overline{u_i}k\right)=\frac{\partial}{\partial x_i}\left(\frac{\nu_t}{Pr_k}\frac{\partial k}{\partial x_i}\right)-\overline{u_i' u_j'}\frac{\partial \overline{u_j}}{\partial x_i}-\varepsilon+\overline{S}_{k,p,s}+\overline{S}_{k,p,v} \tag{5}$$

$$\frac{\partial \varepsilon}{\partial t}+\frac{\partial}{\partial x_i}\left(\overline{u_i}\varepsilon\right)=\frac{\partial}{\partial x_i}\left(\frac{\nu_t}{Pr_\varepsilon}\frac{\partial \varepsilon}{\partial x_i}\right)-C_{\varepsilon 1}\frac{\varepsilon}{k}\overline{u_i' u_j'}\frac{\partial \overline{u_j}}{\partial x_i}-\left(C_{\varepsilon 2}+\frac{C_\mu \eta^3\left(1-\eta/\eta_0\right)}{1+\beta\eta^3}\right)\frac{\varepsilon^2}{k}+\overline{S}_{\varepsilon,p,s}+\overline{S}_{\varepsilon,p,v} \tag{6}$$

where

$$\eta=S\frac{k}{\varepsilon} \tag{7}$$

The variables μ, Γ, S, and Pr denote the viscosity, diffusivity, magnitude of the vorticity and the turbulent Prandtl number respectively. The quantities η_0, $C_{\varepsilon 1}$, $C_{\varepsilon 2}$ and β are model constants. The influence of the dispersed phase on the fluid motion is treated as an extra force exerted on the carrier gas. Thus, the momentum transfer from the dispersed phase to the carrier phase is included by adding a reaction force to the Navier-Stokes equations which acts as a surface force on the droplet. This model is known as force coupling model or particle-source-in-cell (PSI-Cell) model proposed by Crowe et al. [22]. The source terms $\overline{S}_{\psi,p,s}$ and $\overline{S}_{\psi,p,v}$ that characterize the direct interaction of mass, momentum, turbulence, energy and species between the droplets and the carrier gas are given in detail in [10] and [23].

Evaporation and dispersion models

Acetone droplets are captured using the Lagrangian procedure. All numerical parcels are tracked by solving their equations of motion only for the drag and gravitation forces. The Root Mean Square (RMS) values of the fluid parcel velocity should be modeled at the droplet location to quantify the instantaneous fluid velocity of the droplets and its effect on the droplet dispersion. This can be adequately done using a stochastic Lagrangian process. The model used in this work is the Markov-sequence dispersion model [10]. It is based on computing the fluid element's instantaneous fluctuation along the particle trajectory using two correlation factors, the Lagrangian and Eulerian, denoting the time and spatial correlation functions, respectively. To avoid the phenomena of droplet immigration to locations having low pressure, a drift correction term was considered [10]. The Uniform Temperature (UT) model by Abramson and Sirignano [10] was applied to evaporation. This model is based on the film thickness theory. The UT model describes the evolution of the droplet temperature and diameter, i.e. evaporation rate and energy flux through the liquid/gas interface. Non-equilibrium effects were included in the evaporation model.

BML extension / croup combustion modeling

Since evaporating droplets travel a distance of 215 mm before reaching the edge of the pilot flow nozzle, the combustion of acetone vapor is shown to promote lean premixed, and diffusion flame. The mixture between the carrier air and the vapor exhibit a wide inhomogeneity in the physical space. The vapor, released by the spray, necessitates a delay time to ensure gas mixing and compose a burnable mixture. The combustion of partially prevaporized droplets is likely to display a partially premixed flame behavior. Therefore, the Bray-Moss-Libby (BML) model was extended and adapted to capture the spray combustion. The transport equation for the progressive variable, given by Equation (1), was solved.

$$\frac{\partial(\bar{\rho}\tilde{c})}{\partial t}+\frac{\partial(\bar{\rho}\tilde{u}_j\tilde{c})}{\partial x_j}=\frac{\partial}{\partial x_j}\left(-\bar{\rho}\widetilde{c''u_j''}\right)+\widetilde{\dot{w}_c}\,, \tag{8}$$

where c denotes the progress variable and is defined as:

$$c=\frac{T-T_u}{T_b-T_u}\,. \tag{9}$$

In Equation (9), u is the unburned and b the burnt part of the flame. Equation (8) contains the mean reaction rate term, which is modeled as:

$$\widetilde{\dot{w}_c}=\rho_u s_L^0\left(C_L\frac{k^{3/2}}{\varepsilon}\right)^{D-3}\left(\frac{\nu^{3/4}}{\varepsilon^{1/4}}\right)^{2-D}\tilde{c}(1-\tilde{c})\,, \tag{10}$$

where the constant C_L is 0.41 in all simulations and the fractal dimension D is set to 7.7/3. The results of conditioned combustion products must be multiplied by the probability p^b of being behind the flame font to extract the physical products.

$$Y_\alpha(z,p^b)=Y_\alpha^b(z)\,p^b\,, \tag{11}$$

In the context of the BML model, this probability can be directly related to the progressive variable c so that

$$Y_\alpha(z,p^b)=Y_\alpha^b(z)\,c\,. \tag{12}$$

Assuming a bimodal PDF of c, it can be shown that

$$\tilde{Y}_\alpha\left(\tilde{c},\tilde{z},\widetilde{z''^2}\right)=\tilde{c}\widetilde{Y_\alpha^b}\left(\tilde{z},\widetilde{z''^2}\right)\,. \tag{13}$$

In addition to the Favre-averaged equations of continuity, momentum and turbulent quantities, a Favre-averaged mixture fraction equation $\tilde{z}$ and a Favre-averaged equation for its variance $\widetilde{z''^2}$ have to be considered. The Favre-averaged equation for the mixture fraction can be written as:

$$\frac{\partial\bar{\rho}\tilde{z}}{\partial t}+\frac{\partial(\bar{\rho}\tilde{u}_i\tilde{z})}{\partial x_i}=\frac{\partial}{\partial x_i}\left(\rho D\frac{\partial\tilde{z}}{\partial x_i}-\bar{\rho}\widetilde{u_i''z''}\right)+\tilde{S}_{\tilde{z},p}\,. \tag{14}$$

After neglecting the molecular diffusion terms, the final closed equation for mixture fraction variance yields to:

$$\frac{\partial\bar{\rho}\widetilde{z''^2}}{\partial t}+\frac{\partial\left(\bar{\rho}\widetilde{u_i}\widetilde{z''^2}\right)}{\partial x_i}=\frac{\partial}{\partial x_i}\left(\bar{\rho}\frac{\nu_t}{S_{ct1}}\frac{\partial\widetilde{z''^2}}{\partial x_i}\right)+2\bar{\rho}\frac{\nu_t}{S_{ct2}}\frac{\partial\tilde{z}}{\partial x_i}\frac{\partial\tilde{z}}{\partial x_i}-c\,\bar{\rho}\frac{\varepsilon}{k}\widetilde{z''^2}+\tilde{S}_{\widetilde{z''^2},p} \tag{15}$$

When droplet vaporization occurs due to the local sources of fuel, the mixture fraction z is not a conserved scalar. It results in two additional source terms ($\tilde{S}_{\tilde{z},p}$ and $\tilde{S}_{\widetilde{z''^2},p}$) appearing in the transport equation of $\tilde{z}$ and $\widetilde{z''^2}$. The source terms $\tilde{S}_{\tilde{z},p}$ and $\tilde{S}_{\widetilde{z''^2},p}$ for the mixture fraction (and its variance) are given by [11] as follows:

$$\tilde{S}_{\tilde{z},p}=-\sum_p\frac{\dot{m}_{p,v}N_p}{V_{i,j,k}}\,, \tag{16}$$

and

$$\tilde{S}_{\widetilde{z''^2},p}=\left(-\sum_p\frac{\dot{m}_{p,v}N_p}{V_{i,j,k}}\right)\frac{\widetilde{z''^2}(1-2\tilde{z})}{\tilde{z}}\,. \tag{17}$$

Since the injected parcels demonstrate a relatively high density number around the configuration axis, the combustion and vaporization are influenced by the presence of multiple droplets within a considered control volume. Droplets interact with the environment and among themselves. This interaction, which is referred in the literature as group effect, prevents air penetration to the dense zones that are formed by droplet clouds. The latter may develop rich areas that feature non-flammable mixture. Figure 1 shows multiple forms of droplet accumulations that display an external group combustion behavior. The presence of group combustion in the studied configuration is mainly located at the center of the jet and close to the nozzle exit. The group effect reflects different mode of spray combustion. Chiu et

al [12] classified these modes to external sheath combustion, external group combustion, internal group combustion and single droplet combustion, see Figure 2. For the determination of the nature of the group combustion occurring in the used configuration, the group combustion number, G, was determined. G represents the ratio of the heat transfer in the gas phase and the heat transfer between two phases accounting for connective effects. The group combustion number, G, is given as follows:

$$G = 3\left(1 + 0.276\,\mathrm{Re}^{1/2}\,Sc^{1/3}\right) LeN\left(\frac{r_p}{R_b}\right), \tag{18}$$

where *Re, Sc* and *Le* are the droplet Reynolds, Schmidt and Lewis numbers respectively. *N* represents the total number of droplets present in the cloud, r_p is the droplet radius and R_b is the droplet cloud radius. Numerically, the cluster of droplets was assigned to the considered control volume (cv). N is the droplet number within the cv. The variable r_p is the mean droplet radius and $R_b = (vol)^{1/3}$. Figure 3 displays the variation of the group combustion number along the central axis of the configuration. The experimental value of G varies between 0.3 and 4.03. The determined values of G indicate that an external group combustion mode is likely to appear in the acetone spray combustion.

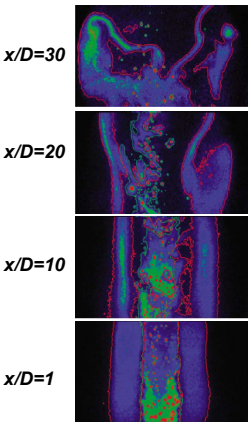

Figure 1: Acetone/OH LIF [13]

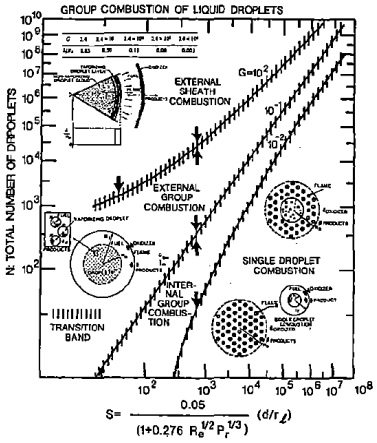

Figure 2: Group combustion modes of a droplet cloud [12]

The collective behavior of the droplets influences the temperature of the vapor that mixes with surrounding heated gas. The vapor exhibits a gradual transition from the droplet surface temperature to the environment condition. Figure 4 shows both, the surface droplet temperature and the gas temperature at the tracked parcel location. At the beginning of the tracking, the gas temperature equals the value given at the Boundary Condition (BC), i.e. 300K. It increases promptly when the droplet reaches the vicinity of the flame. In contrast the droplet surface temperature does not pass the boiling temperature. The vapor temperature lies between both extremes. For the determination of thermodynamic properties of the air-vapor mixture while modeling the evaporation process, the 1/3 rule was applied. I.e. film properties were evaluated using 1/3 of the surrounding gas conditions and 2/3 of the droplet surface conditions. This rule was also applied to determine the acetone vapor temperature that is needed for the computation of the progress variable reaction source term. Indeed, the increase of the vapor temperature should be taken into account while determining the laminar burning velocity of acetone. Metghalch and Keck mentioned in there work [14] and more extensively Dahoe and de Goey [15] expressed the dependency of the laminar burning velocity on the temperature and pressure of the mixture as a polynomial function.

$$s_L(p,T) = s_L(p_0,T_0)\left(\frac{T}{T_0}\right)^m \left(\frac{p}{p_0}\right)^n, \tag{19}$$

where $s_L(p_0,T_0)$ represents the burning velocity at the reference temperature and pressure condition (p_0,T_0). For the used study, the laminar acetone burning velocity, as recently published by Pichon at al. [16], at atmospheric pressure and room temperature (298K) is applied.

Figure 5 shows $s_L(p_0, T_0)$ as function of the equivalence ratio. The flammability limits are approximately 0.7 for the lean composition and 1.6 for the rich. The parameter *m*, and *n* denote the temperature and pressure exponents that are dependent of the fuel used. Since the operating pressure *p* is identical with the reference pressure p_0 the exponent *n* is not relevant for the determination of the laminar burning velocity. The exponent *m*, is experimented by Molkov and Nekrasov [17] and set to 1.28 for acetone.

For the generation of the flamelet table, A detailed chemical reaction mechanism for acetone is used. The reaction mechanism is developed and validated by Pichon et al. [16]. It involved 84 species and 409 reactions. The Lewis number is not set to the unity, yet for every species a Lewis number is assigned. And the strain rate is set to 100/s. A presumed β-*pdf* is considered to generate the look up table.

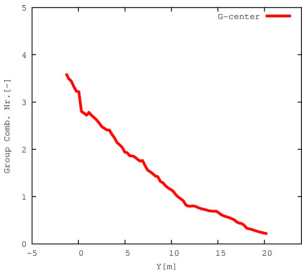

Figure 3: G decay along the centerline

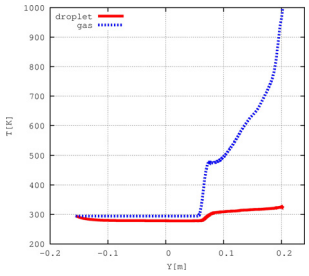

Figure 4: Sample of a droplet/Gas temp. variation

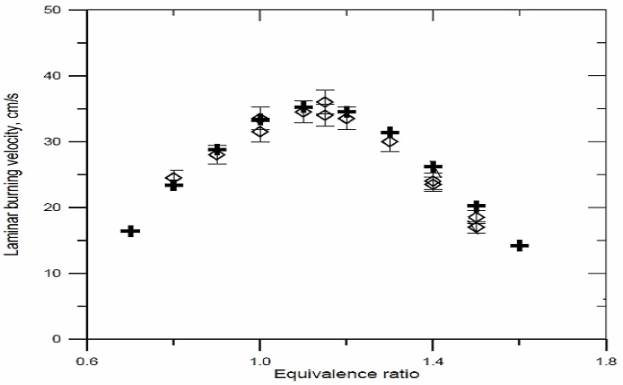

Figure 5: New measurements of laminar burning velocities of acetone + air mixture at atm. pressure and room temp. (298K): Pichon et al. [16]

Configuration and boundary conditions

A detailed description of the experimental setup and apparatus used for the generation of the experimental data is given in Starner et al [13] and Masri and Gounder [18]. The geometry of the configuration used to study the acetone spray evaporation and/or combustion is shown in Figure 6. The burner is mounted vertically in a wind tunnel that supplies a co-flowing air stream of 4.5 m/s. The co-flow is provided within a diameter of 104 mm. The pilot flame that is set to a stoichiometric mixture of hydrogen, acetylene and air has an unburnt bulk velocity of 1.5 m/s. The spray is initialized 215 mm upstream of the nozzle exit plane.

Table 1 shows the investigated configuration details for SP1/AcF1, SP2/AcF2 and SP5/AcF5. A deceasing mass loading $\dot{m}_l / \dot{m}_{tot}$ in the inner jet is recorded. It equals 33.33%, 25% and 19.95% for the different test cases respectively. The turbulent kinetic energy of the carrier phase is given 5% of the bulk velocity at the inlet.

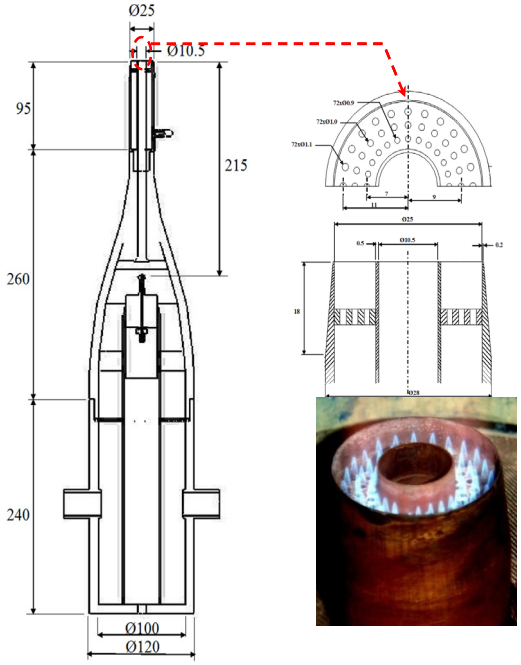

Figure 6: Configuration of the acetone spray burner [19].

Table 1: Different test cases with the flow BC

Test case description	***SP1 / AcF1***	***SP2 / AcF2***	***SP5 / AcF5***
$\dot{m}_l\,[g/\min]$	75	75	75
$U_{jet}\,[m/s]$	24	36	48
$\dot{m}_{air}\,[g/\min]$	150	225	301
$\mathrm{Re}_{jet}\,[-]$	24417	32131	39609

The simulations are performed using 12 different classes of droplets. Figure 7 shows the Probability Density Function of the droplet number for each class. Droplets having diameter higher than 80 µm yield negligible number, yet their mass flow rate is important. This is due the correlation of droplet mass with the third exponent of the diameter, e.g. three times bigger droplets include 27 times more mass. Figure 8 shows the mass flow rate distribution for each droplet class. Giving exact BC for the classes with dp > 80 µm is extremely crucial for the disperse phase properties and the progress of combustion at the late sampling sections. Indeed larger droplets endure the long travel distance, survive the flame front and release their vapor within the heated environment.

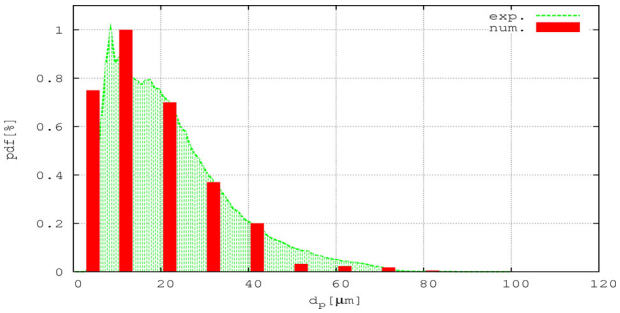

Figure 7: PDF of the droplet number. Num. BC vs. exp.

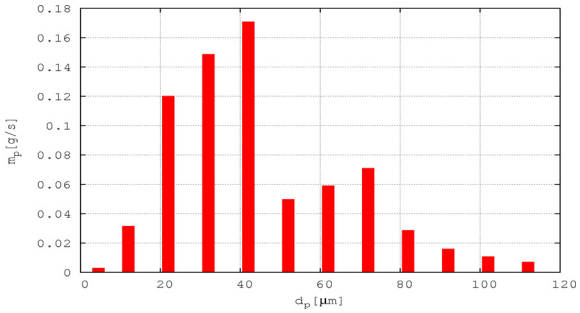

Figure 8: Mass flow rate distribution per class

Figure 7 shows the distribution of the droplet classes, given numerically, and compared it to the experimental data. Figure 9 shows the axial droplet velocity and its fluctuations for one test case (SP5/AcF5). It is remarkable that almost all classes possess the same injection axial velocity that equals 42 m/s, whereas the standard deviation corresponds to ca. 3 m/s yielding an axial turbulence intensity of 7.5%. The radial component is shown in Figure 10. The radial velocity, v_p, is less than 2.5 m/s and goes to zero at the axis because of the symmetry condition. The fluctuation $v_p^{'}$ is remarkably important if compared to v_p.

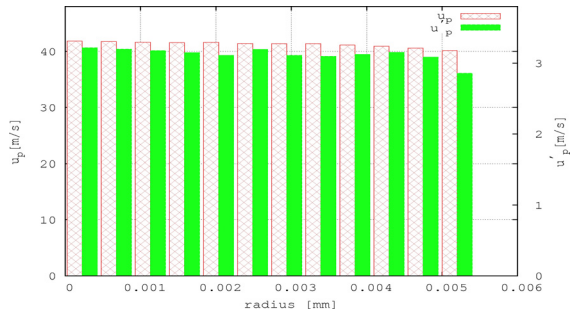

Figure 9: Axial droplet velocity and its fluctuations.

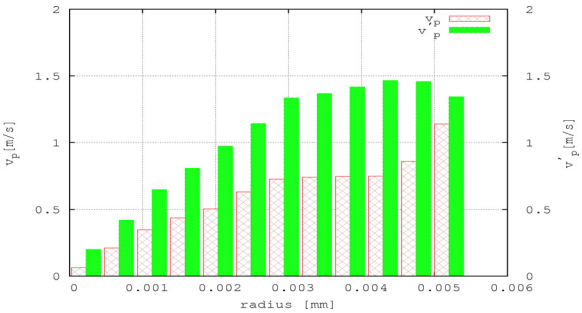

Figure 10: Radial droplet velocity and its fluctuations.

The computational domain consists of 17 blocks that count 553774 control volumes. The total number of the numerical tracked droplets exceeded 1 millions parcels within one coupling-iteration, thus the results are proven to be statistically independent. Indeed the profiles of the droplet characteristics feature PDF moments that are not conditioned by the droplet number within the control volume. The convergence of the Eulerian-Lagrangian coupling procedure is reached when the fluid's properties do not change their value from one coupling to the next in the presence of droplets. Unfortunately, there are no universal guidelines for selecting criteria because they depend not only on the physical processes being approximated but also on the details of the numerical formulation.

Results and discussion

The Mean droplet axial velocities are plotted for Non-reacting and reacting test cases in Figure 11. Very good agreement between numerical prediction and experimental measurements is observed. The velocity curves feature a smooth profile hinting to statistically independent results, i.e. the number of numerical parcels used within each coupling reveals enough samples to deliver profiles that are independent to the injected parcels. The increase of the jet velocity maximums for the test cases Sp1 to Sp5 is due to the augmentation of the carrier phase mass flux at the boundary conditions. The Droplet axial velocity in the reacting test cases (AcF1, AcF2 and AcF5) yields higher values starting from x/D=10 downstream, because of the acceleration caused by the density jump which is located at the combustion zone, between x/10=10 and x/10=20. Noteworthy is that droplets are distributed over the entire cross section in the non-reacting test case starting from x/10=15 downstream. The reacting cases show, however, spray presence only till r/D=1. This is caused by the high carrier phase temperature at r/D=1, as will shown in Figure 17. The profiles of the axial droplet velocity give a hint about the spray opening angle which reveals to be in a good agreement with the experimental data. The trend of the radial profile of the droplet axial velocities is similar for the three test cases. The increase of the carrier phase volume flux, i.e. decrease of the two phase flow loading, is remarkable through the augmentation of the droplet axial velocity.

Figure 12 shows the standard deviation of the droplet axial velocities where disagreements are observed at the early cross sections. Indeed the numerical simulations under predict the fluctuations of the spray axial velocity in the vicinity of the nozzle exit plane. The discrepancy seen there is mainly originated to the failure of numerical models at predicting the bimodality of the spray behavior at the edge of the exit nozzle. Gounder and Masri showed in [19] that the spray yielded a mono-modal at the jet centerline and gradually shifts to a bimodal distribution as the jet wall is approached. This effect generates a wide range of droplets having large and small diameter, thus demonstrating a wide range of stokes number. Small droplets follow the carrier phase which is highly turbulent and anisotropic due to the geometry featured by the configuration at the nozzle exit plane which is similar to that of a bluff body. Larger droplets, however, impose their momentum and may yield important slip velocities. Thus the fluctuation of droplet velocity is large at the nozzle edge, where the bimodality was observed. In order to capture this phenomenon, the numerical simulation should include coalescence and brackup models. The remaining cross sections show acceptable agreements except for the SP5 test case where the disagreement could be correlated to the mean axial velocity profiles. Decreasing the two-phase flow loading worsen the statistics. Note that by increasing the gas phase velocity, the droplet axial velocity fluctuation increase as well. Indeed the flow becomes more turbulent and the droplets dispersion is more important. The reacting cases show an increasing trend of the fluctuation profiles with respect to radius. This behavior is opposite to the cold test cases.

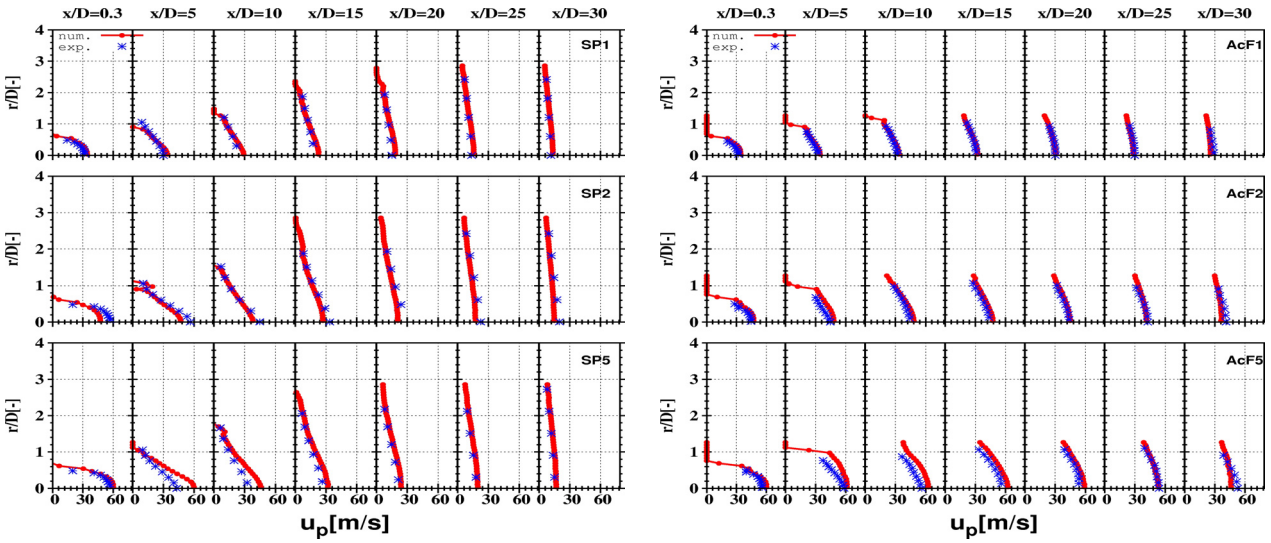

Figure 11: Droplet axial mean velocity for different loading, at different axial cross sections. Left = non reacting test cases (Sp1, Sp2 and Sp5). Right= reacting test cases (AcF1, AcF2 and AcF5)

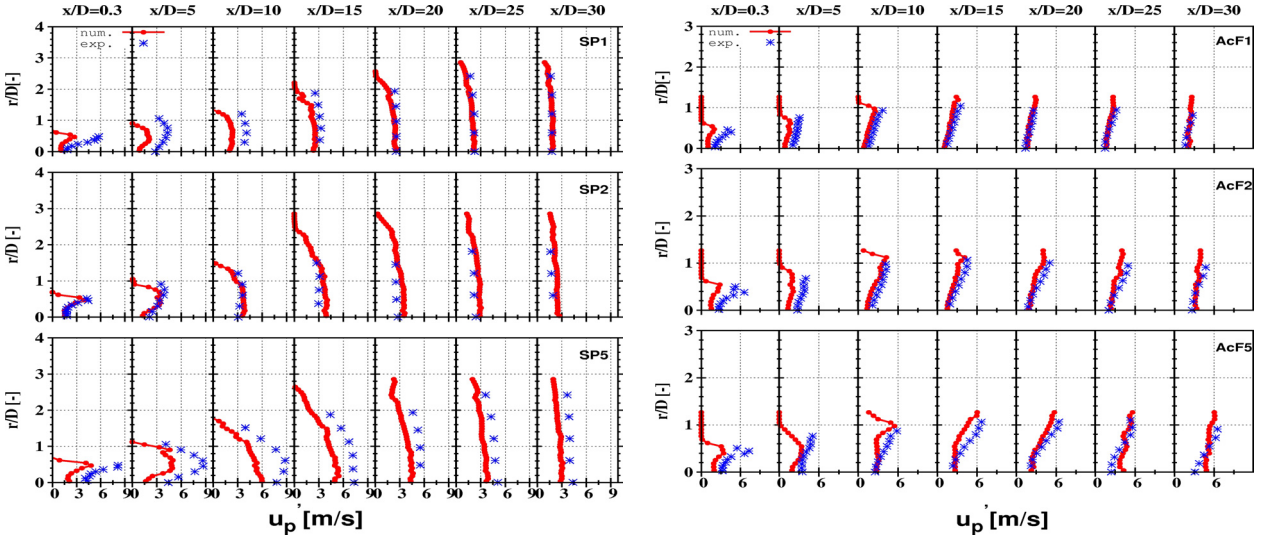

Figure 12: Droplet axial velocity fluctuations for diff. loading, at diff. axial cross sections. Left = non reacting test cases (Sp1, Sp2 and Sp5). Right= reacting test cases (AcF1, AcF2 and AcF5)

Figure 13 and Figure 14 illustrate the radial mean velocity profiles and its fluctuations respectively, at different distances from the nozzle exit plane. Regions viewing a zero velocity, e.g. toward the co-flow, are caused by the absence of the disperse phase. Cells of the computational domain that contain no droplets display zero values for the dispersed phase properties. The profiles demonstrate small discrepancies which are within the experimental error range. The magnitude for both, i.e. mean velocities and fluctuations, show an increasing trend from Sp1/AcF1 to Sp5/AcF3 which is explained by the different inlet mass flux of the carrier phase. It is worth mentioning that the fluctuations are of the same order of magnitude as the mean values. The radial velocity at x/D=0.3 is negligible because of the interaction with the nozzle edge. Further downstream, the spray is distributed more homogenously, and the droplets disperse horizontally yielding a uniform profile for the evaporating cases. However, droplets show an increasing radial velocity profile in the reacting condition. Discrepancies in Figure 13 (right) may be originated from the measurements, since the profiles do not demonstrate the symmetry condition that impose zero velocity at the axis.

In the transition region, between loaded ($r/D<1$) and unloaded two-phase flow ($r/D>1$), the numerical profiles shows wrinkled curves which are also originated at having not enough

parcels within a considered control volume. This effect is more pronounced for the AcF5 since the loading is decreased as the inlet velocity of the carrier phase was increased. The augmentation of the numerical number of tracked droplets did not improve the statistics nor improve the smoothness of the curves. The disagreement at the velocity fluctuations could also be explained by the presence of droplet that featured mainly large diameter. They have their own dynamic and do not follow the gas phase. The dispersion model should be further investigated with respect to the dense two-phase flow. Moreover, the droplet formation and coalescence effects should be considered at this dense region.

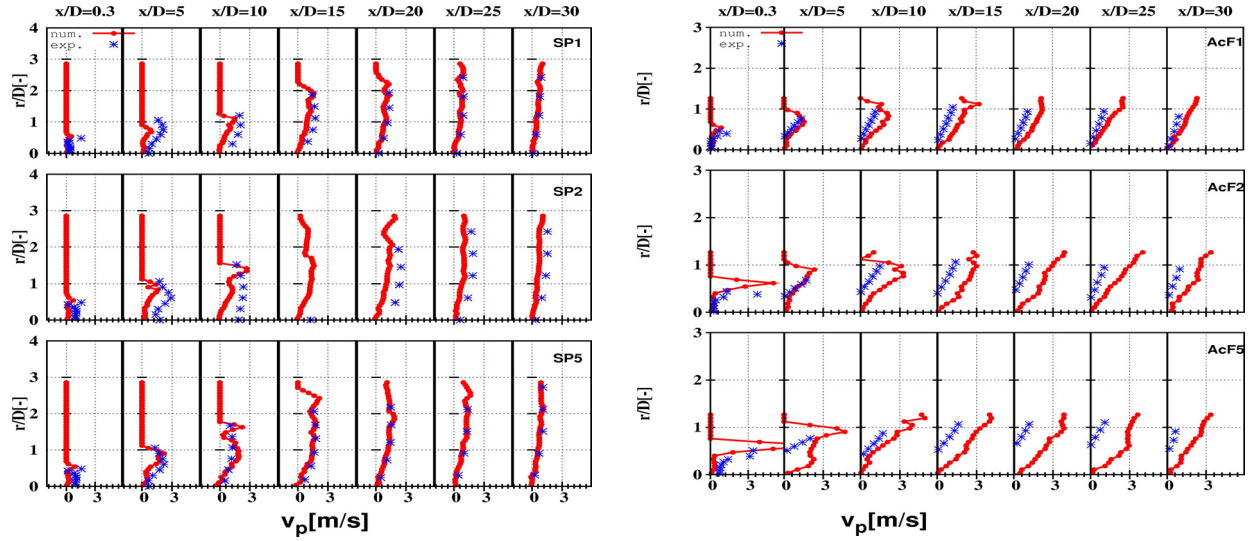

Figure 13: Droplet radial mean velocity for different loading, at diff. axial cross sections. Left = non reacting test cases (Sp1, Sp2 and Sp5). Right= reacting test cases (AcF1, AcF2 and AcF5)

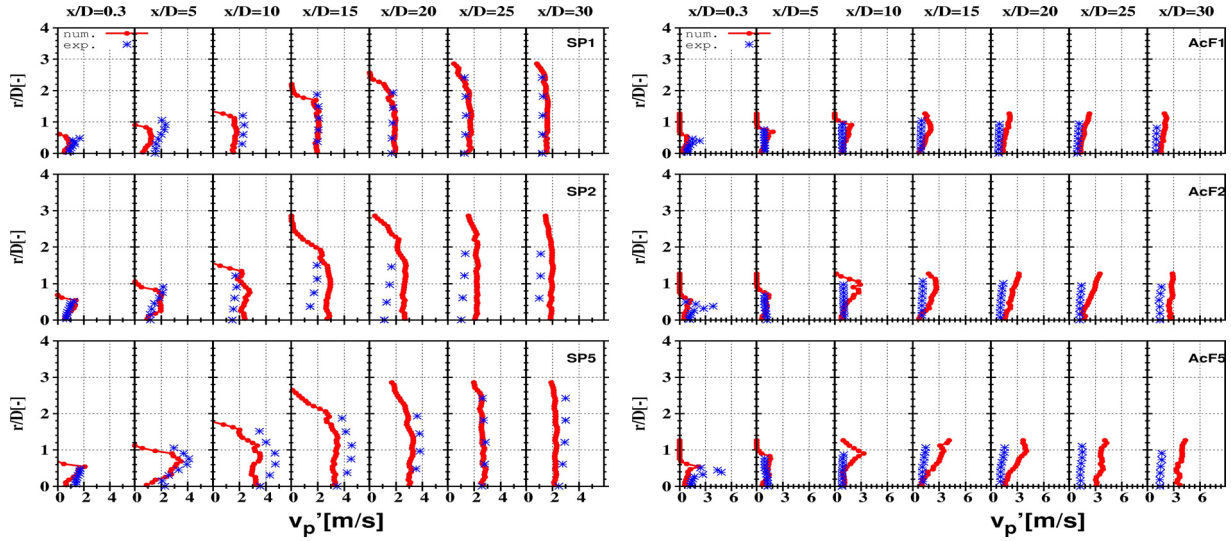

Figure 14: Droplet radial velocity fluctuation for diff. loading, at diff. axial cross sections. Left = non reacting test cases (Sp1, Sp2 and Sp5). Right= reacting test cases (AcF1, AcF2 and AcF5)

Figure 15 shows the radial profile of the mean droplet diameter of all classes. The agreement between the numerical simulation and the experimental data is good for the first six cross sections. While traveling downstream the mean droplet diameter increases despite mass losses due to evaporation. This is caused by vanishing of small classes. In fact, small droplets evaporate within the travel distance $x/D < 10$, and only bigger parcels survive till the last section. It is worth to notice that large droplets are located at the edge of the spray jet ($r/D=1$) for the reacting cases. The profiles of the droplet diameter reveal that the mass

loading does not affect the diameter distribution. The influence of the flame on the spray mean diameter is observed on the increasing trend of the profiles. In the centerline, the droplets show nearly constant value. In this region, the carrier phase has cold temperature.

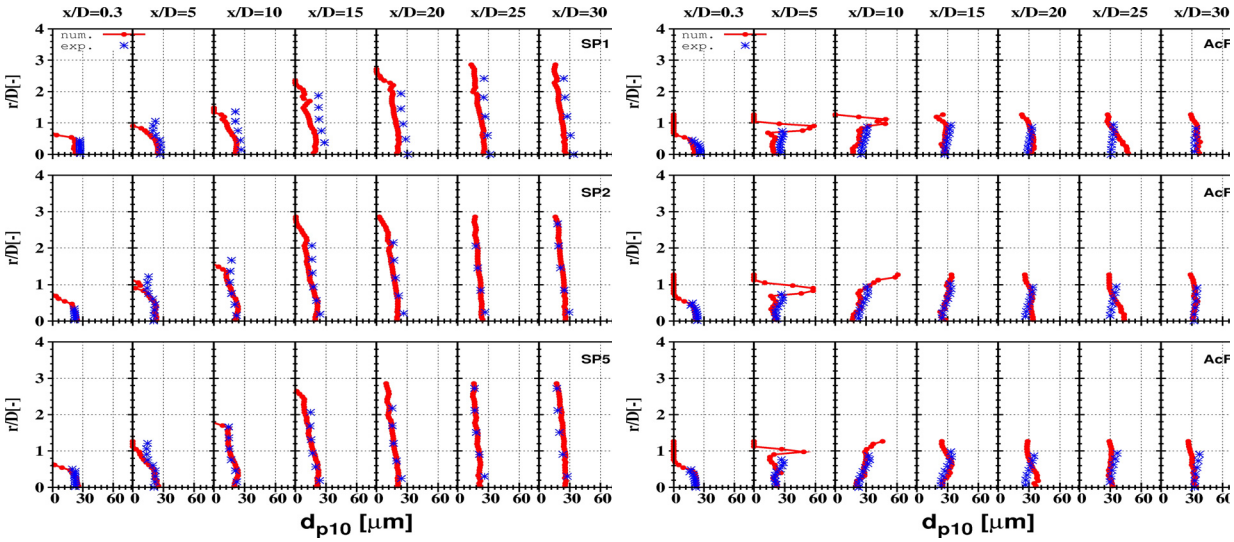

Figure 15: Droplet mean diameter for different loading, at diff. axial cross sections. Left = non reacting test cases (Sp1, Sp2 and Sp5). Right= reacting test cases (AcF1, AcF2 and AcF5)

Figure 16 displays the spray mass flux profiles, which is a reliable indicator of the evaporation rate validation. The spray is mainly evaporated when reaching x/D=20. Only droplets of the 10^{th}-12^{th} classes pass this cross section. These droplets build the spray properties at the end of the spray jet. Increasing the carrier phase axial velocity slightly raises the spray mass flow rate. Indeed droplets are dragged faster and do not have sufficient time to evaporate and release mass to the surrounding environment. Capturing the exact evaporation is very crucial for the correct prediction of the combustion process. Disagreement beyond x/D=15 is not very relevant for the combustion since the majority of droplets, when reaching this cross section, have already evaporated upstream. The phase transfer is mainly determined by the low droplet classes whose life time is the smallest and evaporate notably faster than the larger droplet classes. The non-equilibrium evaporation model has shown better results than the equilibrium one. Indeed, effects of non-equilibrium thermodynamics are present during the evaporation because of the high turbulence level and the elevated temperature gradients for the reacting cases. The non-equilibrium conditions are mainly present when the evaporation rate is higher. This situation is corresponds to the droplet size since the smaller is a droplet, the higher is the ratio of surface to diameter, i.e. the Sauter diameter, thus the phase transition will be enhanced. This condition, which is being stronger at the end of the droplet life time, is perfectly fulfilled by applying the (neq.) evaporation model. By accounting for (neq.) effects, the surface vapor mass fraction is decreasing (due to the deviation factor placed in the vapor mole fraction equation), this will consecutively reduce the mass transfer Spalding number. The diminution of the Spalding number causes an augmentation of the modified Sherwood number that represents, physically, the correction of the evaporation rate due to the presence of Stefan flow. The evaporation is therefore enhanced because of the diminishing of the droplet diameter where the (neq.) conditions are developing accordingly. The second condition for non-equilibrium evaporation processes, which is present within reacting test cases, is the prompt changing on the temperature of the liquid gas interface. This situation is detected when droplets leave the pre-vaporization zone and approach to the flame front, thus they are faced to a very high temperature gradient, and thereby the droplet properties have not enough time to relax toward its thermodynamic equilibrium. Subsequent to the injection, the

spray begins to change its phase only because of the existing vapor gradient between the droplet surface and fresh inlet air. As a consequence, the carrier phase decreases its temperature due to the evaporation. The later effect was, however, not carried out due to the adiabatic flamelet table generation used for the simulation of the combustion processes. Further downstream the spray approaches the combustion zone and starts experiencing the high flame temperature that enhances the vaporization.

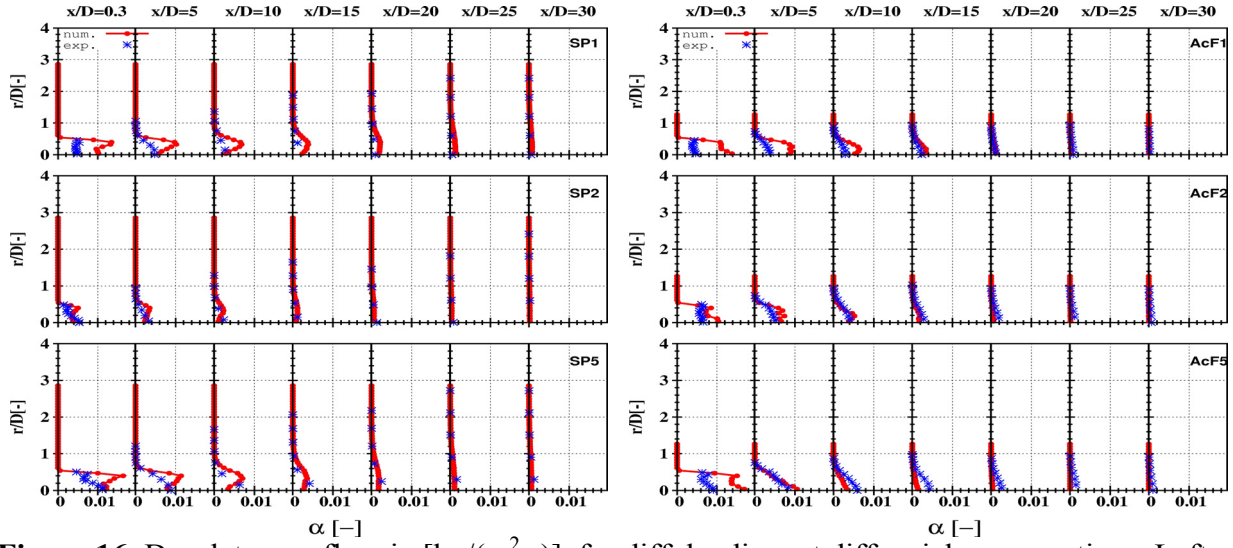

Figure 16: Droplet mass flux, in [kg/(m^2.s)], for diff. loading, at diff. axial cross sections. Left = non reacting test cases (Sp1, Sp2 and Sp5). Right= reacting test cases (AcF1, AcF2 and AcF5)

Figure 17 shows the mean temperature profiles of the acetone spray combustion for the different inlet velocities. The trend is well predicted, however discrepancies are observed primarily at the last cross section. This could be due to the heat losses due to radiation, which were not accounted for and/or to the measurements error since the later were performed using thermocouple element, whose sensitivity is accordingly important at elevated temperature. The simulated flame breadth is in agreements with experimental findings. It is worth mentioning that by increasing the carrier phase velocity, the flame become broader and shorter. These effects are more pronounced in the numerical results. The over prediction of the temperature, may be caused by the disagreement seen at the mass flow rate or by using single (strain rate) flamelet table. By increasing the flame strain rate, the flame move toward non-equilibrium chemistry and the maximum temperature is going to reduce. By using Flamelet Generated Manifold table, FGM, the temperature agreements can be improved. The trend of the temperature augmentation at the centerline at *x/D=10* with increasing the gas phase mass flow rate is obvious for the numerical simulation. In contrast, the experimental data shows a temperature decrease at the AcF5 test case. The increase of the gas phase inlet velocity makes

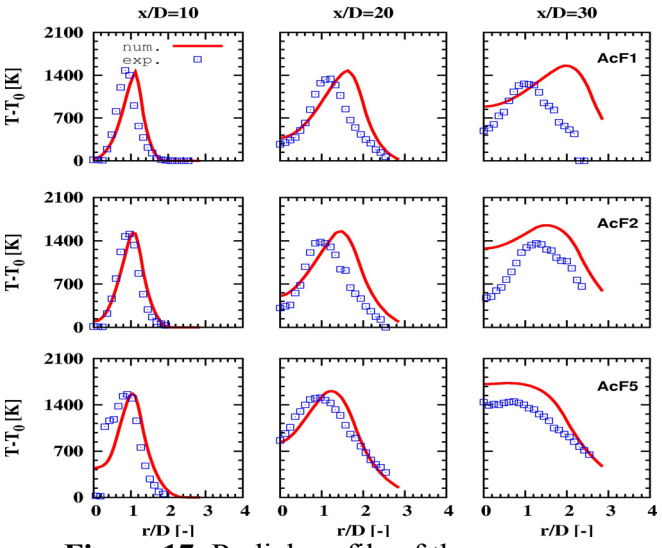

Figure 17: Radial profile of the gas mean temperature at diff. axial cross section for the test cases AcF1, AcF2 and AcF5

the flow more turbulent which in turn enhance the reaction rate. The peak of the flame temperature is located at the jet edge where the fuel rich zone interacts with the fresh co-flow. It is also observed that the flame lift off is reduced with increasing air flow rate.

Conclusion

Acetone spray behavior is studied for reacting and non-reacting turbulent two phase flow. Numerical results are plotted vs. experimental data. Good agreements are observed for the mean axial velocity, however discrepancies are noticed for the second moments, which were correlated to the spray interaction with the nozzle edge. The global model for the two phase flow includes sub-models for the dispersion, turbulence modulation and polydispersity. The Bray-Moss-Libby model is extended for simulating spray combustion. Non-equilibrium evaporation along with RANS turbulence models are used and a fully two way coupling is accounted for. Further investigations should be put on the wall spray interaction and the droplet formation as well as four way coupling at the dense flow region, e.g. close to the nozzle exit. The mean droplet diameter and the spray mass flow rate are in acceptable agreement. The temperature profiles demonstrated a good trend. Yet it could be improved by using variable strain rates, i.e. Flamelet Generated Manifold. The BML model well captured the flame breadth and lift off. The group combustion effect that influences the laminar burning velocity has an important impact on the determination of the progress variable and therefore the position of the flame front. It is worth mentioning that at high temperature thermocouples used in the experiment may exhibit larger errors. . Because of the multiple physical phenomena that occur in the spray combustion, further validation with different fuel that exhibit different thermo dynamical and chemical properties is necessary.

References

[1] H. W. Ge and E. Gutheil, Comb. & Flame Vol. 153, pp 173-185, April 2008
[2] I. Düwel, et al., Proc. Comb. Inst., Vol. 31, pp 2247-2255, Jan. 2007
[3] H. Watanabe, et al., Comb. & Flame Vol. 148, pp 234-248, March 2007
[4] C.-H. Tsai, S.-S. Hou, and T.-H. Lin, Comb. & Flame Vol. 144, pp 277-288, January 2006
[5] N. Patel and S. Menon, Comb. & Flame, Vol. 153, pp 228-257, April 2008
[6] F. Akamatsu, et al., Int. Symp. on Comb., Vol. 26, pp 1723-1729, 1996
[7] M. Mortensen, and R. W. Bilger, Comb. & Flame, Vol. 156, pp 62-72, January 2009
[8] S. K. Marley, et al., Experimental Thermal and Fluid Science, Vol. 29, , pp 23-31, Dec. 2004
[9] C. Pichard, Y. Michou, C. Chauveau, Gökalp, Proc. Comb. Inst., Vol. 29, pp 527-533, 2002
[10] M. Chrigui, A Sadiki, J. Janicka, Hage, A. Dreizler, Atom.&Sprays, 19(10):929-955, (2009).
[11] M. Chrigui, et al., Experimental Thermal and Fluid Science, Vol. 34 pp 308-315,2010
[12] H.H. Chiu, H.Y. Kim, E.J. Croke, Symp. (Int.) on Comb., Vol. 19, pp 971-980, 1982
[13] S. H. Stårner, J. Gounder, and A. R. Masri, Com. & Flame, Vol. 143, pp 420-432, Dec. 2005
[14] M. Metghalchi, and J. C. Keck, Com. & Flame, Vol. 48, pp 191-210, 1982
[15] A. E. Dahoe, L. P. H. de Goey, J. of Loss Pre. in the Proc. Ind., V. 16, pp 457-478, Nov. 2003
[16] S. Pichon, et al., Com. & Flame, Vol. 156, pp 494-504, Feb. 2009
[17] V.V. Molkov and V.P. Nekrasov. Comb. Explosion, Shock Waves, Vol. 17, pp 280-283, 1981
[18] A. R. Masri and J.D. Gounder, Proc. of the 6th Mediterranean Com. Symp., 2009
[19] J. D. Gounder and A. R. Masri, ICLASS, July 2009
[20] Crowe, C. T "Multiphase Flow Handbook", ISBN-10: 0849312809, section 12 page 116
[21] M. Chrigui, A Sadiki, J. Janicka, Hage, A. Dreizler, Atom.&Sprays, 19(10):929-955, (2009).
[22] C. T., Crowe, M. P. Sharma, & , D. E. Stock, J. Fluids Eng. June. (1977).
[23] M. Chrigui, J. of computational thermal science, Vol. 2, Issue 1, pp 55-78, (2010).